Structure and properties of an Al alloy in as-cast state and after laser treatment

Mariusz Król[*], Przemysław Snopiński, Błażej Tomiczek, Tomasz Tański,
Wojciech Pakieła, and Wojciech Sitek

Division of Material Processing Technology, Management and Computer Techniques in Materials Science, Institute of Engineering
Materials and Biomaterials, The Silesian University of Technology, ul. Konarskiego 18a, 44-100 Gliwice, Poland

Abstract. This work is focused on thermal analysis, metallurgical characterization, and laser treatment of an aluminium alloy. This paper contributes to a better understanding of non-equilibrium metallurgical character of aluminium alloys. The solidification of the aluminium dendritic network, the aluminium–silicon eutectic and iron- and magnesium-containing intermetallic phases are characterized. The influence of laser treatment on the structure and properties of the aluminium alloy was also determined. Moreover, to improve the mechanical properties and wear resistance of the surface layer, the tested alloys were subjected to surface treatment using a HPDL laser and simultaneous feeding of tungsten carbide particles into the molten pool of the EN AC-51500 aluminium alloy.

Key words: aluminium alloy, manufacturing, processing, casting, thermal analysis, laser treatment.

1. INTRODUCTION

Currently there are an enormous number of construction materials, but the demands placed on them are growing. Therefore, much time-intensive research is conducted to develop new and better materials and technologies. Aluminium alloys are the second most commonly used materials after steel, being mainly used in the aerospace and automotive industries. Nowadays the primary challenge these industries face is reduction of carbon dioxide emission. Thus, it is necessary to use new, lighter materials. In the United States, Europe, and China, which are the greatest producers of cars, the priority issue is to reduce the total weight of the finished product through the use of lighter, more durable materials, and thereby reduce CO_2 emissions into the atmosphere. By 2020, China plans to decrease the amount of fuel combustion by up to 5 L per 100 km. In Europe, the plan is to reduce

CO_2 emissions into the atmosphere to 95 g/km. In the United States, a reduction of CO_2 emissions to a level of 101 g/km is expected by 2025. The new generation of cars is convincing evidence of such efforts. For example, the 4th generation of the Golf, one of the most popular Volkswagen models sold in the world, weighed 1163 kg. After 15 years, the 7th generation, which is much better equipped, both in the security systems and devices that increase comfort, weighs only 1150 kg. This is ensured by the use of modern materials, including the increased use of hot-formed steel from 5% to 20% and innovative solutions [1–3].

Aluminium alloys that combine low density and high strength are increasingly used in applications where weight reduction of components is necessary and cost-effective [1]. It is expected that the use of aluminium alloys will increase, despite competition from polymeric materials and composites [2–4]. Consequently, it is necessary to develop high-strength alloys with better properties and higher corrosive resistance [5–8]. Castings

---

[*] Corresponding author, mariusz.krol@polsl.pl

that contain different cross-section thicknesses result in various cooling rates, which, in turn, affect the as-cast structure. To adequately control microstructure development during melting, solidification, and other types of materials processing it is necessary to understand all metallurgical phenomena that take place. Knowledge of the crystallization process, as well as of the influence of liquid and/or semi-solid metal treatment on the micro- and macro-structure, is of primary importance [9–11].

Thermal derivation analysis has a very broad scope in both research and industrial practice. It is possible to perform thermal analysis on an alloy just before casting into the mould to carry out any adjustments to the quality of molten metal, for example for subsequent heating or cooling. Obtaining so much information of interest in a very short time (2–5 min) allows for an immediate decision to improve the quality or causes an elevated technical discipline process. Therefore, such analysis is the best and easiest way to improve the quality of foundry and to make decisions about the degree of the reliability of machines and equipment [9–17].

2. EXPERIMENTAL PROCEDURE

2.1. Material

The investigations were carried out on the casting aluminium alloy EN AC-51500 (hereafter 51500 alloy). Its chemical composition is presented in Table 1.

2.2. Thermal analysis

The thermal analysis of the melting and solidification cycles was carried out using the Universal Metallurgical Simulator and Analyser (UMSA) [18]. The scheme of the device and dimensions of the specimens were described in [12,13]. The data for thermal analysis (TA) were collected using a high-speed National Instruments data acquisition system linked to a personal computer. For temperature measurement, a chromel-alumel thermocouple was applied (with the extra low thermal time constants), placed in a thermal node in the middle of the sample. Each TA trial was repeated three times for each of the three samples. The TA signal in the form of heating and cooling curves was recorded during the melting and solidification cycles. Temperature versus time and first derivative versus temperature were calculated and plotted. Accurate information concerning phase transformations

is necessary to perform computer simulations of casting feedability and characterization of the solidification process, as well as to make predictions concerning the cast structure.

The α-Al dendrite nucleation temperature ($T^{\alpha DEN}_{NUC}$), α-Al dendrite minimum (undercooling) temperature ($T^{\alpha DEN}_{MIN}$), α-Al dendrite coherency point ($T^{\alpha DEN}_{DCP}$), α-Al dendrite growth temperature ($T^{\alpha DEN}_{G}$), Al–Mg$_2$Si eutectic nucleation temperature ($T^{AlSi}_{E,NUC}$), Al–Mg$_2$Si eutectic minimum temperature ($T^{AlSi}_{E,MIN}$), Al–Mg$_2$Si eutectic growth temperature ($T^{AlSi}_{E,G}$), and solidus temperatures T_{SOL} were calculated using the first derivative of the cooling curve [15–17].

The characteristic points were estimated as follows: $T^{\alpha DEN}_{NUC}$ – the intersection of the tangent to the straight stretch of the crystallization curve to the base line, $T^{\alpha DEN}_{MIN}$ – the first derivative of the cooling curve reaches a zero value, $T^{\alpha DEN}_{DCP}$ – the second derivative of the cooling curve reaches a minimum of zero, $T^{\alpha DEN}_{G}$ – the first derivative reaches zero again, the temperature of the Al$_{15}$(FeMn)$_3$Si$_2$ phase – the intersection of the tangent drawn to the straight line of the differential curve, $T^{AlSi}_{E,MIN}$ – the first derivative of the cooling curve reaches a zero value, $T^{AlSi}_{E,G}$ – the first derivative reaches zero again, and T_{SOL} – the point where the ends of multi-component eutectic crystallization occur and where the alloy is fully crystallized. The cooling rate (CR) was calculated based on the following relationship:

$$\mathrm{CR} = \frac{T^{\alpha DEN}_{NUC} - T_{SOL}}{\Delta t}, \qquad (1)$$

where Δt is crystallization time. This cooling rate corresponds approximately to the cooling of casting in sands.

The Newtonian base line

$$(\mathrm{d}T/\mathrm{d}t)_{BL} = a_0 + a_1 T + a_2 T^2 + a_3 T^3 + a_4 T^4 + a_5 T^5 + a_6 T^6 \qquad (2)$$

was estimated by the sixth polynomial fitting between the beginning and the end of solidification in the crystallization curve. The sixth order polynomial yields a correlation coefficient equal to 0.99. Based on characteristic marks from the thermal analysis, the heat of individual phases of phase transition was calculated.

The heat capacity c_p of the metal was measured using the following equation [17]:

$$c_p(t) = c_{p\,SOL} \int_{t_N}^{t} f_S(t)\,\mathrm{d}t + c_{p\,LIQ}\left(1 - \int_{t_N}^{t} f_S(t)\,\mathrm{d}t\right), \qquad (3)$$

where $c_{p\,SOL}$ and $c_{p\,LIQ}$ designate heat capacity in solid and liquid state, respectively, and f_S is participation of fraction solid, considering that for $f_S(t \leq t_N) = 0$ and $f_S(t \geq t_N) = 1$.

Table 1. Average chemical composition (wt%) of the 51500 Al alloy

Fe	Si	Cu	Zn	Ti	Mn	Mg
0.12	1.9	0.005	0.01	0.009	0.58	5.17

The specific heat capacity in the liquid and the solid state was determined using Thermal-Calc software. The total heat of the crystallization process of the analysed alloys was calculated based on the following formula:

$$Q = c_p m \int_{t_N}^{t_{SOL}} \left[\frac{dT}{dt} - \left(\frac{dT}{dt} \right)_c \right] dt. \qquad (4)$$

2.3. Laser treatment

To improve the wear resistance and mechanical properties of the top surface of the aluminium alloy tungsten carbide (WC) particles have been used. The size of the applied powder has been in the range from 45 to 200 μm. To aid the melting of the modified surface, the high power diode laser (HPDL) has been used [19–22]. The HPDL is characterized by a very high power density of the laser beam under standard conditions of up to 10^7 W/cm² [23]. This ensures that the thermal impact on the component is limited and thus causes only minor thermal stress and strain [24–26]. The WC powder has been introduced into the molten pool using feeder gravity content of 8 g/min. To limit diffusion, laser treatment has been carried out in Ar inert gas [25–27]. Tribological and mechanical properties of the composite layer have been analysed by the measured hardness and 'ball on plate' wear test [28].

2.4. Microstructure examinations

Metallographic specimens were obtained from a location close to the thermocouple tip. To reveal the structure, a polished section was etched using Keller's etchant. Microstructure features were characterized using a light optical microscope (Leica Q-WinTM image analyser). The X-ray qualitative and quantitative analyses and the examination of the surface distribution of the cast elements and the shape, size, and distribution of WC particles in the examined aluminium cast alloy were performed on the scanning electron microscope ZEISS SUPRA 35 with an EDAX XM4 TRIDENT system consisting of EDS, WDS, and EBSD spectrometers. The X-ray examinations of the investigated aluminium alloy were made using an X'Pert Pro diffractometer with a Cu anode. Diffraction analyses were performed within the range of angles from 20° to 90°. The measurement step was 0.05° in length and the pulse counting time was 5 s.

3. RESULTS AND DISCUSSION

3.1. Thermal analysis

The representative heating and cooling curve of the 51500 alloy solidifies without interruption, by a quench, as presented in Fig. 1 for a typical metallurgical
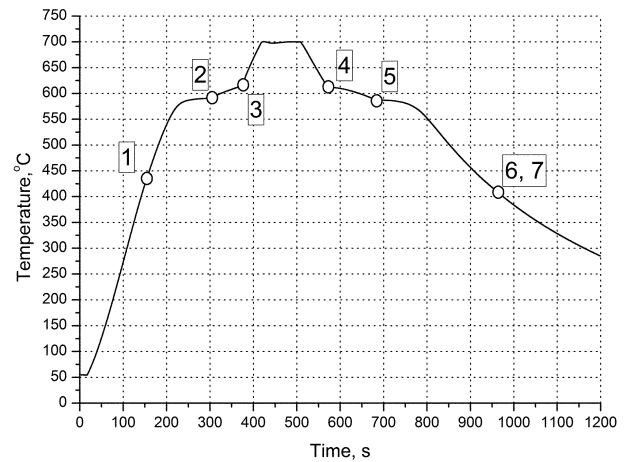
Fig. 1. Representative heating and cooling curve of the 51500 aluminium alloy.

reaction for this alloy. For non-equilibrium heating and cooling, significant differences can be observed between heating and cooling metallurgical results, i.e. $\Delta T = T^{\alpha DEN}_{NUC} - T_{SOL} \approx 22\,°C$. The temperature shift between heating and cooling events (the so-called metallurgical hysteresis) is caused by the non-equilibrium heating and solidification process. This information is of paramount importance because many published papers wrongly use data of solidification thermal analysis for the determination of the quality of a melt batch via recording phase change temperatures and fraction solid-temperature profiles. Definitions and measured values of the characteristic points associated with individual non-equilibrium metallurgical events taking place during both melting and solidification processes shown in Fig. 1 are presented in Tables 2 and 3.

The thermal (metallurgical events) are not clearly visible in Fig. 1. Therefore, the first derivative is needed for a precise determination of curve characteristics (Fig. 2). As can be observed, the alloy does not begin to solidify immediately at the equilibrium solidification temperature because no sufficient nuclei are present.

Some undercooling is needed to supply the driving force for the nucleation and growth of the aluminium dendrites. Latent heat evolves and causes the temperature of the surrounding melt to rise. With further melt cooling,

Table 2. Thermal characteristics of the heating cycle for the analysed aluminium alloy (heating rate 0.8 °C/s)

Point	Stage	Temperature, °C
1	Beginning of melting process	436.5 ± 1.2
2	Melting of Al–Mg–Si eutectic	592.02 ± 1.7
3	End of melting process	619.69 ± 1.9
Melting time		183.2 ± 6 s

Table 3. Thermal characteristics of the cooling cycle for the analysed aluminium alloy (cooling rate 0.5 °C/s)

Point	Stage	Temperature, °C
4	Nucleation of Al dendrite network (liquidus temperature)	616.14±0.9
5	Nucleation of Al–Mg–Si eutectic	589.08±2.4
6	Nucleation of Mg enriched and other phases	434.48±2.1
7	End of alloy solidification process (solidus temperature)	414.08±2.3
Solidification time		202.06±12 s
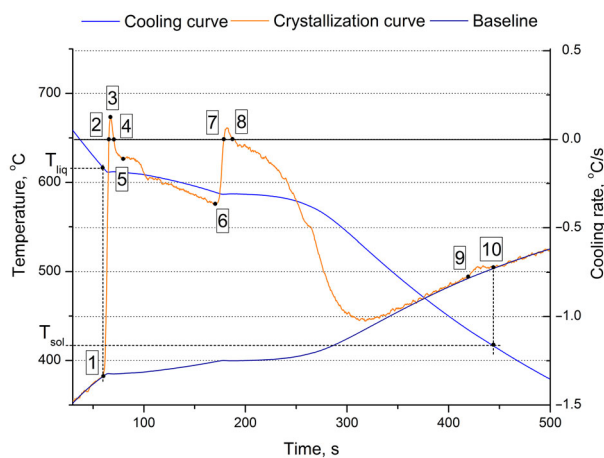
Fig. 2. Representative cooling, crystallization, and base curves with characteristic points of the crystallization process of the 51500 aluminium alloy solidifying at 0.5 °C/s.

the dendrites continue to grow. Based on the first derivative (Fig. 2), $T^{\alpha DEN}_{NUC}$ (point 1), which represents the temperature at which the first stable dendrites start to solidify from the melt, was found to be 616.14 °C. The liquidus temperature is the point where the fraction solid begins, and the solid fraction at this point is equal to zero.

The next characteristic point on the crystallization curve was observed at 611.52 °C, that is at $T^{\alpha DEN}_{MIN}$ (point 2), which outlines the state where the nucleated dendrites have grown to such an extent that the liberated latent heat of fusion balances the heat obtained from the test sample. At point 3 the created α dendrites in the liquid melt become coherent ($T^{\alpha DEN}_{DCP}$). At that point, another derivative of the cooling curve crosses the zero line. The $T^{\alpha DEN}_{DCP}$ was noted at 611.72 °C. After crossing that point, the melt temperature rises to a steady state growth temperature $T^{\alpha DEN}_{G}$ (point 4). This event was observed at 611.98 °C.

During the crystallization process, the next characteristic point was found at 611.24 °C, which relates to the next metallurgical reaction due to the precipitation

of $Al_{15}(FeMn)_3Si_2$ (point 5). Based on the first derivative curve, it can be observed that the solidification rate (dT/dt, °C/s) begins to slow down to almost zero, which is a result of the larger latent heat of the eutectic phases formed by Mg_2Si and α-aluminium. As a result of the continuous cooling of the aluminium alloy, $T^{AlSi}_{E,NUC}$ is 589.08 °C (point 6). The $T^{AlSi}_{E,NUC}$ represents the Al + Mg_2Si eutectic nucleation temperature at which a stable nucleation of coprecipitating Mg and Si crystals and then Al from the interdendritic melt begins to form cells that start to grow.

At 586.73 °C $T^{AlSi}_{E,MIN}$ occurs (point 7), which is characterized by a next local minimum on the cooling curve and is defined as the time when the first derivative crosses the zero line following the Al–Si nucleation temperature (dT/dt = 0). The next local temperature during the crystallization process is noted at 587.13 °C (point 8), which on the first derivative curve is $T^{AlSi}_{E,G}$. Nucleation of the Al_3Mg_2 enriched phases (point 9) was observed at 434.48 °C and solidus temperature T_{SOL} (point 10), where the crystallization process is finished, was at 414.08 °C.

Figure 3 and Tables 4 and 5 present data on the thermal analysis of the aluminium alloy during solidification at a cooling rate of 0.5 °C/s. The crystallization sequence is influenced to a considerable extent by the
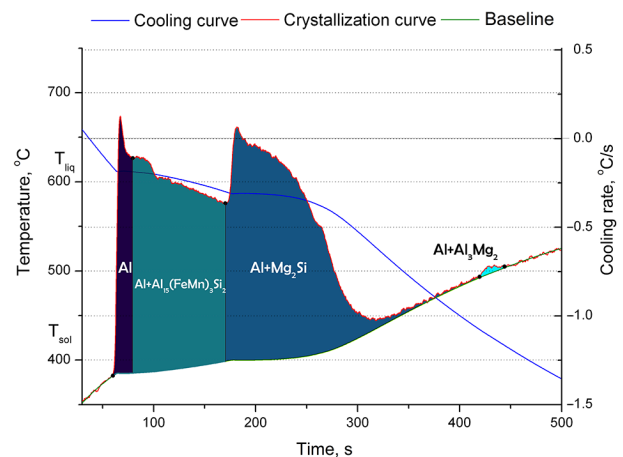
Fig. 3. Thermal analysis data of the 51500 Al alloy during solidification at a cooling rate of 0.5 °C/s. Areas of the crystallization of individual components are marked.

Table 4. Heat capacity of the 51500 aluminium alloy in liquid and solid states

Specific heat in liquid state $c_{p\,LIQ}$, J/g·°C	1.08
Specific heat in solid state $c_{p\,SOL}$, J/g·°C	0.9
Weight, g	13.29

Table 5. Latent heat of crystallization of the 51500 Al alloy emitted during solidification and its participation in crystallization at a cooling rate of 0.5 °C/s

Reaction during solidification (temp.)	Latent heat of crystallization process		Participation of latent heat, %
	Per sample	Per 1 g of sample	
L→Al, dendritic network (611.52 °C)	302.9	22.8	9.7
L→Al+Al$_{15}$(Fe, Mn)$_3$Si$_2$ (611.24 °C)	1287.3	96.9	42
L→Al+Mg$_2$Si (589.08 °C)	1482.1	111.5	48.1
L→Al+Al$_3$Mg$_2$ (434.48 °C)	7.8	0.6	0.2
Total	3080.1	231.8	100

presence of iron and manganese. These elements, together with aluminium and silicon, start to precipitate just after the formation of the dendritic network. Solidification begins with the formation of a dendritic network of aluminium, which is immediately followed by the precipitation of Al$_{15}$(FeMn)$_3$Si$_2$.

The precipitation of the Al$_{15}$(FeMn)$_3$Si$_2$ phase continues down to the quasi-ternary eutectic reaction, where it keeps precipitating into the Mg$_2$Si phase. Based on the binary alloy system Al–Mg, the final result with a small thermal effect belongs to the precipitation of the Al$_3$Mg$_2$ phase.

The Al–Mg–Si phase diagram suggests that the investigated alloy should contain (α-Al + Mg$_2$Si + β-Al$_3$Mg$_2$) phases, where the morphology of β-Al$_3$Mg$_2$ is relevant for the mechanical properties of the alloy. The selected typical structures of the 51500 alloy obtained in a light microscope are shown in Fig. 4.

Analysis of the microstructure indicates that the examined material consists of an α-Al solid solution matrix (dark matrix) with Mg$_2$Si (bright precipitate) and
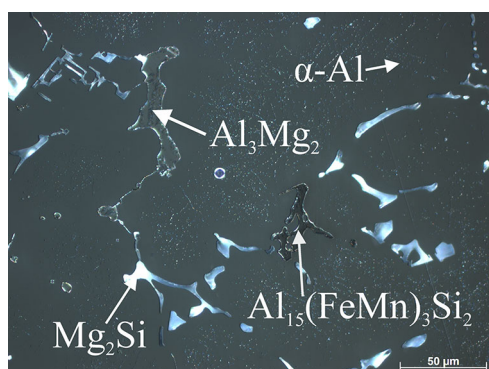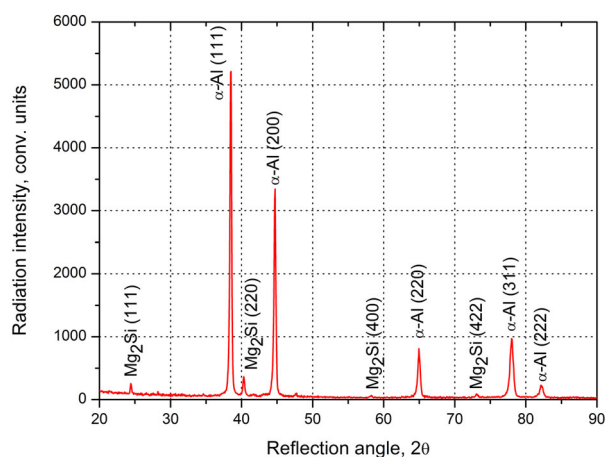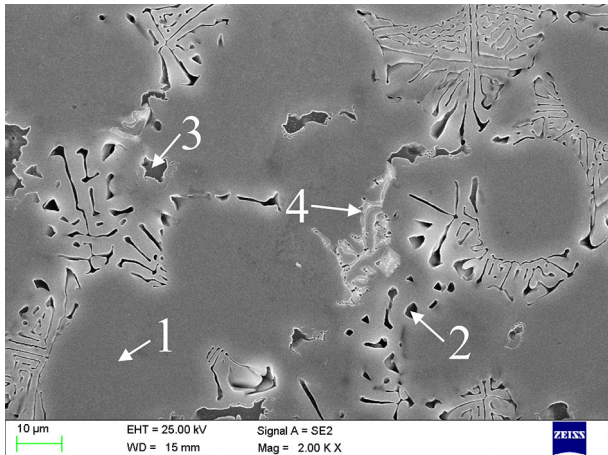
β-Al$_3$Mg$_2$ (brown precipitate), which are located on grain boundaries. Slight precipitates of irregular shape, which probably are cubic Al$_{15}$(FeMn)$_3$Si$_2$, were also observed near the Mg$_2$Si phase. In Al–Si unmodified and slowly solidified cast components made from hypoeutectic alloys, the eutectic silicon crystals grow in a faceted manner in the form of large brittle flakes, which can be observed in Fig. 4.

It is hard to make a precise identification of intermetallics using only one method (e.g. microscopic examination); therefore the XRD method was used to ensure confidence in the results of phase identification based on the metallographic study. Figure 5 shows diffraction patterns of the examined alloy in the as-cast state and cooled at a rate assumed in the experiment. Examination of the X-ray phase showed the presence of the Mg$_2$Si phase and α-Al, which is an alloy matrix, as confirmed by the metallographic study. A scanning electron microscope (SEM) micrograph combined with spot X-ray microanalysis for the 51500 cast after thermal analysis, performed to identify the morphology of the observed phases, is presented in Fig. 6.

An EDS quantitative analysis confirmed the presence of primary alloying elements in the investigated alloy (Table 6). Scanning electron microscopy and quantitative analysis confirmed the presence of the eutectic phase $\alpha + \beta$ and Mg$_2$Si intermetallic, forming a characteristic particle shape called the 'Chinese script'. In addition, using EDS analysis, the occurrence of phases containing Mn and Fe was found. The stoichiometric composition is similar to the Al$_{15}$(FeMn)$_3$Si$_2$ phase. The stoichiometry of Fe-bearing particles depends on the Si and Mn amounts. Iron usually combines with Si and Al to form Al$_8$Fe$_2$Si or Al$_{12}$FeSi in low Mg content alloys or Al$_3$Fe in the absence of Mg. In case of an increased amount of Mn, other particles may be present, such as Al$_{15}$(Fe,Mn)$_3$Si$_2$ and Al$_6$(Fe,Mn).

Fig. 4. Microstructures of the 51500 alloy solidified at a cooling rate of 0.5 °C/s, magnification ×500.

Fig. 5. X-ray diffraction pattern of the 51500 aluminium alloy.

Fig. 6. Representative scanning electron microscope micrograph of the 51500 aluminium alloy solidified at 0.5 °C/s.

Table 6. Pointwise chemical composition analysis from Fig. 6

Point	Element	Mass concentration of main elements, %	
		weight %	atomic %
1	Mg	3.5	3.9
	Al	96.4	96
2	Mg	5.4	6.
	Al	86.6	86.4
	Si	7.9	7.5
3	Mg	29.5	31.8
	Al	70.5	68.1
4	Mg	2.3	2.8
	Al	68.3	76.5
	Si	1.7	2.1
	Mn	12.3	6.7
	Fe	11.4	6.2

A microhardness test showed that the individual precipitates formed during the solidification process are characterized by different hardness (Table 7). The lowest hardness of about 65 $HV_{0.05}$ was exhibited by the α-Al solid solution and the Mg_2Si phase. The microhardness measurement revealed the presence of phases with high hardness, which causes a strengthening effect in this alloy. The average value of microhardness was about

Table 7. Microhardness of the examined 51500 aluminium alloy after thermal analysis

| Phase	Average microhardness, $HV_{0.05}$
α-Al	64.2 ± 0.5
Al_3Mg_2	117.5 ± 0.9
Mg_2Si	65.3 ± 0.5
$Al_{15}(FeMn)_3Si_2$	172.2 ± 1.3

172 HV, which confirms that hard $Al_{15}(FeMn)_3Si_2$ phases are present in the $AlMg_5Si_2Mn$ alloy. Also, it was observed that the microhardness of small irregular-shaped dark precipitates Al_3Mg_2 was about 117 $HV_{0.05}$. The hardness measurement carried out using the Rockwell method showed that the alloy (after the remelting process) was characterized by lower hardness (74.46 HRF after remelting, 81.15 in as-cast state). This could be caused by the microporosity formed during solidification.

3.2. Laser treatment

Deposition of tungsten carbide on the top surface of the aluminium alloy matrix allowed the obtaining of a hard layer with improved wear resistance. A large part of the introduced particles of tungsten carbide powders broke apart. Decomposition of the initial powder to small particles less than 1 μm is distributed according to the direction of convection movements in the molten pool, thereby improving the mechanical and tribological properties of composite layers.

Undissolved particles were mostly on the surface or sedentary on the bottom of the molten pool. Decomposition was not observed in the particles in the central part of the layers. The structure of the composite layers after the laser treatment is presented in Fig. 7. Examination of the surface topography of the samples after the laser treatment showed a uniform distribution of undissolved particles and decomposition of initial powder particles on the surface of the metal. Analysis of the cross-section revealed that the tungsten carbide particles were closely associated with the aluminium alloy matrix. No cracks, voids, or pores around the embedded particles were observed, which may indicate a good wettability of the particles by the matrix material. The parameters of the wear test are presented in Table 8. The results of the tribological test confirmed an increase of the wear resistance of the samples with composite layers obtained by the laser treatment.

During the test also the friction coefficient between the tested surface and the ceramic counter specimen was measured. The friction coefficient for samples with tungsten carbide particles embedded in the surface layer was smaller than the friction coefficient of the samples without laser treatment. The friction coefficient for the composite layers was 0.57. The reason for this phenomenon is a smaller friction coefficient between the counter specimens Al_2O_3 and WC powder than between the 51500 aluminium alloy and the counter specimen Al_2O_3. For samples without composite surface layers the friction coefficient was 0.69. The samples with composite layers had lower roughness than the samples of the aluminium alloy without laser treatment. The lowest depth, width, and volume of abrasion were observed for the laser treated materials, which confirms the increase of the wear resistance of the sample with composite layers obtained by the laser treatment.
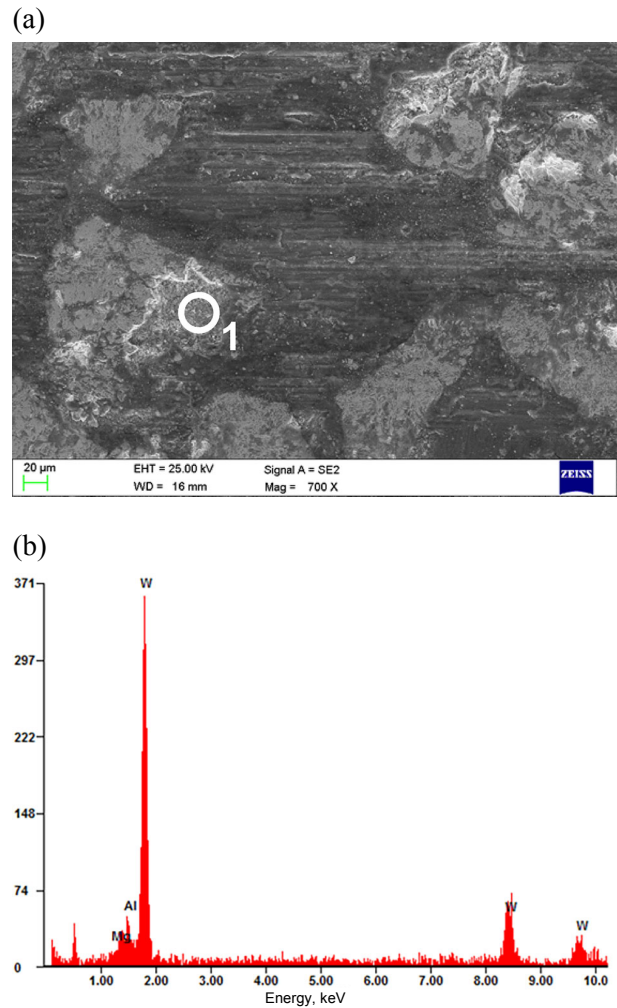
(a)

(b)
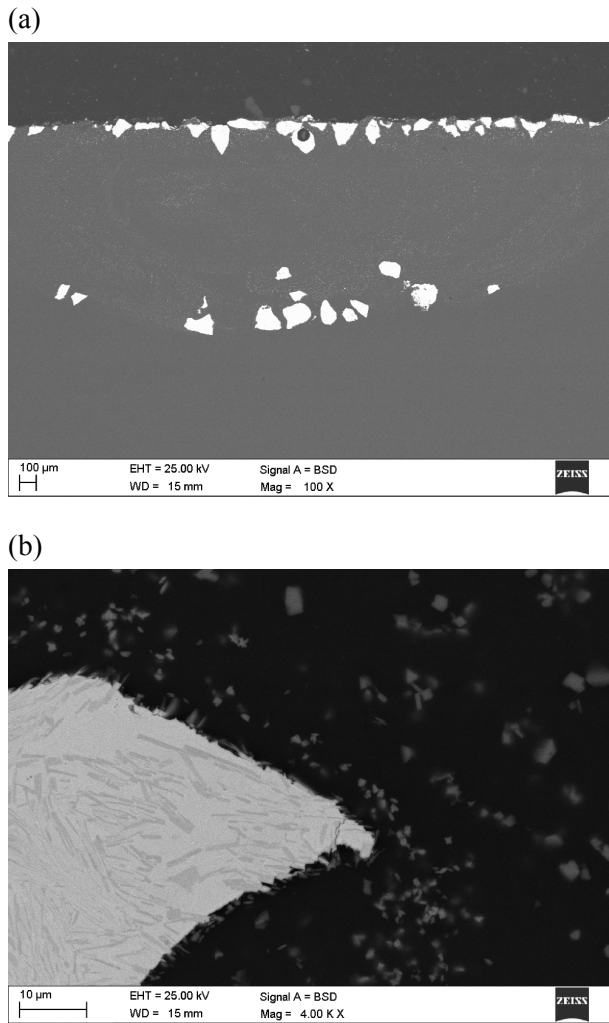
Fig. 7. Structure of the composite layers after the laser treatment with laser beam power of 2.0 kW: (a) solidified molten pool; (b) undissolved particles.

(a)

(b)

Fig. 8. Topography of the wear track after the 'ball on plate' test showing microcuttings and pull-out of incoherent particles from the aluminium matrix (a) and analysis of the chemical composition at a designated point (b).

Table 8. Parameters of the 'ball on plate' wear test

Parameter	Value
Load	5, 7.5, 10 N
Distance	120 m
The length of the test	4 mm
Speed linear motion	5 cm/s

Analysis of the chemical composition of samples using X-ray spectrometry showed that the wear product contained undissolved tungsten carbide particles (Fig. 8b). The mechanism of tearing out incoherent particles of tungsten carbide from the matrix augmented the wear rate of the composite surface layer because the hard particles behave like a microblade increasing surface degradation (m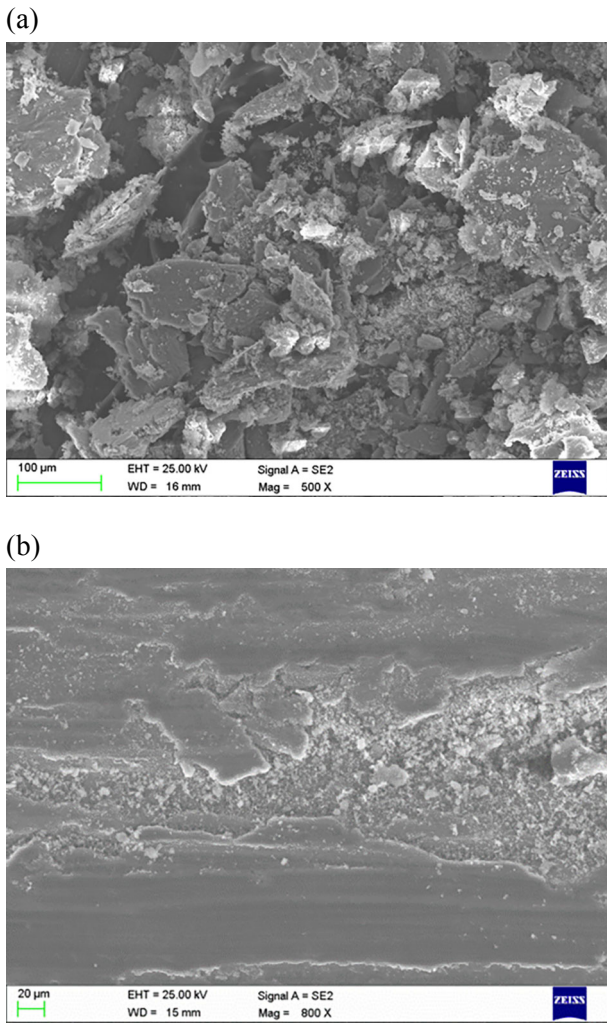icro-cutting). Observation of the wear track after the tribological test showed that the composite layer obtained by the laser treatment was not interrupted (Fig. 8a).
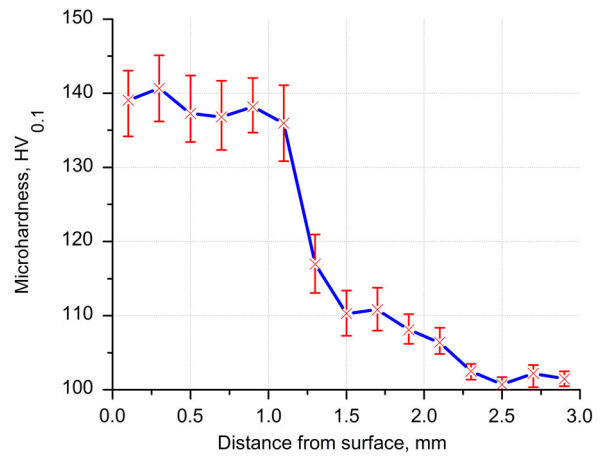
After laser processing the worn samples were observed to have plastically deformed areas and micro-cuttings on the surface, which were caused by the tearing out of tungsten carbide particles from the substrate. Observation of the wear track after the tribological test showed that the composite layer obtained by the laser surface treatment was not interrupted (Fig. 8a).

Analysis of the wear product and the samples without laser treatment showed the presence of large particles detached from the surface of the substrate material (Fig. 9a). This confirms that one of the mechanisms of wear was chipping. The surface of the worn samples without laser treatment has visible traces of losses caused by fissures and signs of material particles torn out from the substrate (Fig. 9b).

(a)

Fig. 10. Microhardness along the cross-section of composite layers obtained by laser treatment.

(b)

Fig. 9. Wear product (a) and wear track of the sample without laser treatment after the 'ball on plate' test with load 5 N (b).

Results of the hardness measurement of the composite layer and base materials showed a significant increase of the hardness of the surface layer to 90 HRF (Table 9). Microhardness measurement along the cross-section of

the solidified molten weld pool showed a significant increase of the hardness at a depth of about 1 mm to about 140 $HV_{0.1}$ (Fig. 10).

4. CONCLUSIONS

The major conclusions drawn from the study are as follows:

- The thermal analysis of the heating cycle permits for the development of an optimum two- and/or multiple-step solution treatment capable of improving the dissolution of the soluble phases (including the Cu-rich ones), which would result in achieving significantly better mechanical characteristics in the thick (slowly solidified) section of the samples.

- The results and parameters obtained from the thermal-derivative analysis can be applied in the metal casting industry for selecting aluminium ingot preheating temperature for semi-solid metal casting (thixocasting, rheocasting, or thixomoulding). The gathered results from TDA ($T^{AlSi}_{E,NUC}$ was up to 10 °C above the

Table 9. Roughness and hardness of the surface and dimensions of the wear track after the 'ball on plate' test

Sample	Load, N	Roughness Ra, μm	Hardness, HRF	Dimensions of the wear profile		
				Depth, μm	Width, mm	Volume, mm³
51500	5	0.37–0.49 (avg 0.47)	77–81	123	1.64	0.5235
	7.5	0.47–0.59 (avg 0.55)	(avg 79)	136	1.74	0.6228
	10	0.51–0.69 (avg 0.57)		149	1.85	0.7568
51500 + WC	5	1.23–1.42 (avg 1.33)	87–95	18	0.69	0.0354
	7.5	0.87–1.11 (avg 0.99)	(avg 92)	20	0.99	0.0396
	10	0.79–0.88 (avg 0.79)		42	1.32	0.0514

eutectic temperature) and microstructure observations confirmed that the aluminium alloy used in the experiment was unmodified.

- Analysis of the microstructure using light and scanning microscopy revealed the presence of an α-Al solid solution matrix with Mg_2Si and β-Al_3Mg_2 that were located on grain boundaries in the interdendritic regions. Additionally it was found that the microstructure also contained hard precipitates of $Al_{15}(FeMn)_3Si_2$ of irregular shape.

- Metallographic analysis of the obtained composite layers confirmed the occurrence of undissolved particles drawn by the convection movements in the bottom solidification molten pool and on the top surface.

- Analysis of samples after laser treatment allows us to state that the resulting layer has a better wear resistance compared to the base material. The obtained results showed a 15 times smaller wear volume of composite layers compared to the aluminium alloy without surface treatment. After laser treatment the resulting layer had a greater hardness compared to the base material (approx. 13 HRF).

ACKNOWLEDGEMENT

REFERENCES

1. Miller, W. Recent development in aluminium alloys for the automotive industry. *Mater. Sci. Eng.*, 2008, **280**(1), 37–49.

2. Krupinski, M., Dobrzański, L. A., Sokolowski, J. H., Kasprzak, W., and Byczynski, G. Methodology for automatic control of automotive Al-Si cast components. *Mater. Sci. Forum*, 2007, **539–543**, 339–344.

3. Holmestad, R., Bjørge, R., Ehlers, F. J. H., Torsæter, M., Marioara, C. D., and Andersen, S. J. Characterization and structure of precipitates in 6xxx Aluminium Alloys. *J. Phys. Conf. Ser.*, 2012, **371**, 012082.

4. Dobrzański, L. A., Tomiczek, B., Pawlyta, M., and Król, M. Aluminium AlMg1SiCu matrix composite materials reinforced with halloysite particles. *Arch. Metall. Mater.*, 2014, **59**(1), 335–338.

5. Tomiczek, B., Pawlyta, M., Adamiak, M., and Dobrzański, L. A. Effect of milling time on crystallite size and microstructure of AA6061 composites fabricated via mechanical alloying. *Arch. Metall. Mater.*, 2015, **60**, 789–793.

6. Tański, T. and Labisz, K. Electron microscope investigation of PVD coated aluminium alloy surface layer. *Solid State Phenom.*, 2012, **186**, 192–197.

7. Tański, T. Characteristics of hard coatings on AZ61 magnesium alloys. *Stroj. Vestn.-J. Mech. E.*, 2013, **59**(3), 165–174.

8. Dobrzański, L. A., Tański, T., and Trzaska, J. Optimization of heat treatment conditions of magnesium cast alloys. *Mater. Sci. Forum*, 2010, **638–642**, 1488–1493.

9. Tański, T., Dobrzański, L. A., and Čížek, L. Influence of heat treatment on structure and properties of the cast magnesium alloys. *Adv. Mat. Res.*, 2007, **15–17**, 491–496.

10. Dobrzański, L. A., Krupiński, M., Labisz, K., Krupińska, B., and Grajcar, A. Phases and structure characteristics of the near eutectic Al-Si-Cu alloy using derivative thermo analysis. *Mater. Sci. Forum*, 2010, **638–642**, 475–480.

11. Dobrzański, L. A, Król, M., Tański, T., and Maniara, R. Thermal analysis of the MCMgAl9Zn1 magnesium alloy. *Arch. Mat. Sci. Eng.*, 2008, **34**(2), 113–116.

12. Król, M., Tański, T., Matula, G., Snopiński, P., and Tomiczek, A. E. Analysis of crystallisation process of cast magnesium alloys based on thermal derivative analysis. *Arch. Metall. Mater.*, 2015, **60**, 2993–2999.

13. Król, M., Tański, T., and Sitek, W. Thermal analysis and microstructural characterization of Mg-Al-Zn system alloys. In *Modern Technologies in Industrial Engineering (ModTech2015)*. IOP Conference Series: Materials Science and Engineering, 2015, **95**, 012006. doi:10.1088/1757-899X/95/1/012006.

14. Dobrzański, L. A., Tański, T., Malara, S., and Król, M. Structure and properties investigation of a magnesium alloy processed by heat treatment and laser surface treatment. *Mater. Sci. Forum*, 2011, **674**, 11–18.

15. Englehardt, H., Hallstedt, B., Drue, M., Loeffler, A., Schick, M., and Rottenmayr, M. Solvus composition paths in multicomponent alloys – experimental approach and correlation with Calphad calculations for the example Al–Mg–Si. *Adv. Eng. Mater.*, 2012, **14**(5), 319–323.

16. Bäckerud, L., Chai, G., and Tamminen, J. *Solidification Characteristics of Aluminum Alloys, Vol. 2: Foundry Alloys*. AFS SkanAluminium, Stockholm, 1990.

17. Tański, T., Labisz, K., Krupińska, B., Krupiński, M., Król, M., Maniara, R., and Borek, W. Analysis of crystallization kinetics of cast aluminum–silicon alloy. *J. Therm. Anal. Calorim.*, 2016, **123**, 63–74.

18. Bäckerud, L., Król, E., and Tamminen, J. *Solidification Characteristics of Aluminum Alloys, Vol. 1: Wrought Alloys*. AFS SkanAluminium, Oslo, 1986.

19. Sokolowski, J. H., Kierkus, W. T., Kasprzak, M. S., and Kasprzak, W. J. (inventors). Method and Apparatus for Universal Metallurgical Simulation and Analysis. US patent, 7,354,491 B2. 2008, Apr. 8.

20. Dobrzański, L. A., Bonek, M., Piec, M., and Jonda, E. Diode laser modification of surface gradient layer properties of a hot-work tool steel. *Mater. Sci. Forum*, 2006, **532–533**, 657–660.

21. Mirski, Z. and Piwowarczyk, T. Analysis of adhesive properties of B2 hardmetal surface. *Arch. Civ. Mech. Eng.*, 2009, **9**(2), 93–104.

22. Węglowski, M., Kwieciński, K., Krasnowski, K., and Jachym, R. Characteristics of Nd:YAG laser welded joints of dual phase steel. *Arch. Civ. Mech. Eng.*, 2009, **9**(4), 85–97.

23. Wiśniewska-Weinert, H., Leshchynsky, V., Ignatev, M., Borowski, J., and Wiśniewski, T. Innovative technology

for fabrication of antiwear layers for forging tools. *Tribologia*, 2011, **5**, 239–248.

24. Klimpel, A. *Laser Technologies*. Silesian University of Technology, Gliwice, 2012.

25. Dobrzańska-Danikiewicz, D., Tański, T., and Domagała-Dubiel, J. Unique properties, development perspectives and expected applications of laser treated casting magnesium alloys. *Arch. Civ. Mech. Eng.*, 2012, **12**(3), 318–326.

26. Dobrzański, L. A., Bonek, M., Hajduczek, E., and Klimpel, A. Application of high power diode laser (HPDL) for alloying of X40CrMoV5-1 steel surface layer by

tungsten carbides. *J. Mater. Process. Tech.*, 2004, **155–156**, 1956–1963.

27. Piec, M., Dobrzański, L. A., Labisz, K., Jonda, E., and Klimpel, A. Laser alloying with WC Ceramic Powder in hot work tool steel using a High Power Diode Laser (HPDL). *Adv. Mat. Res.*, 2007, **15–17**, 193–198.

28. Leschynsky, V., Wiśniewska-Weinert, H., Magda, J., Wiśniewski, T., and Rybak, T. Stanowisko do badań tribologicznych w wysokich temperaturach elementów łożysk z proszków spieków ze zmodyfikowaną warstwą wierzchnią. *Tribologia*, 2010, **4**, 289–292 (in Polish).

Lasertöödeldud valatud Al-sulami struktuur ja omadused

Mariusz Król, Przemysław Snopiński, Błażej Tomiczek, Tomasz Tański, Wojciech Pakieła ja Wojciech Sitek

Artiklis on pühendutud Al-valusulami termoanalüüsile, metallurgilisele iseloomustamisele ja lasertöötlusele ning panustatud eelkõige Al-sulamite mittetasakaalulise oleku metallurgiale. On uuritud alumiiniumi dendriitvõrgustiku, rauda ja magneesiumi sisaldavate intermetalliidsete faaside ning alumiiniumi-ränieutektikumi tardumist. Samuti on välja selgitatud lasertöötluse mõju alumiiniumisulami struktuurile ja omadustele. Parandamaks pinnakihi mehaanilisi omadusi ja kulumiskindlust, kasutati alumiiniumisulami korral laserpinnatöötlust samaaegse volframkarbiidi ette-andmisega sulavanni.